Ultramicroscopy 27 (1989) 375–386
North-Holland, Amsterdam

HREM CONTRAST SIMULATIONS FOR COMPOUND SEMICONDUCTORS – A DISCUSSION OF APPROPRIATE IMAGING PARAMETERS

R. HILLEBRAND and K. SCHEERSCHMIDT

Institut für Festkörperphysik und Elektronenmikroskopie der Akademie der Wissenschaften der DDR, Weinberg 2, Halle DDR-4020, German Dem. Rep.

Received 21 September 1988

In the present paper a method of optimizing HREM imaging parameters is discussed. For crystalline specimens (A_3B_5 semiconductors InP and GaAs) contrast simulations ("multi-slice" algorithm, $V = 400$ kV) are carried out, where the dynamical behaviour of electron diffraction is studied for the (110) and the (100) zone axis. The contrast transfer function is determined to restore the phases of the kinematical structure amplitudes by adapted focusing (KPF). For appropriate specimen thickness ranges and KPF focus the calculated image contrast is interpretable in terms of the projected crystal potential (structural and chemical information).

1. Introduction

High resolution electron microscopy (HREM) has become a very useful tool for investigating structural details of materials on an atomic scale. At present, in the field of semiconducting substances increasing interest is drawn to compound semiconductors. These materials include two or more elements – often in the form of sandwich structures – which are intended to be distinguished as well as localized experimentally by HREM. Electron micrographs of GaAs, InP and related systems, taken preferentially at accelerating voltages of 400 kV, are discussed in the literature (see e.g., refs. [1,2]). It is argued that for very thin crystalline specimens ($t \leq 4$ nm) in $\langle 100 \rangle$ orientation and under imaging conditions near Scherzer focus atom columns are imaged dark, whereas for InP the heavier In atoms appear larger and darker than the lighter P [1].

To obtain "structure images" in the electron microscope the experimental parameters, especially the contrast transfer function (CTF), have to be optimized. In the Scherzer focus, which is correlated with the point resolution of the microscope, interpretable image contrast is obtained for very thin specimens ($\pi/2$ phase shift by CTF). In the so-called "aberration-free focus" (AFF) [3,4], the oscillations of the CTF are fitted to the diffraction pattern of the crystal to prevent any additional phase shift by the electron-optical system. Both concepts fail for compound semiconductor (A_3B_5) materials because of the non-centrosymmetric intensity and phase behaviour in electron diffraction due to dynamical many-beam interactions.

In the present paper a general method of optimizing imaging conditions is discussed. In this attempt the imaging properties of the electron microscope (CTF) are considered in relation to the dynamical electron diffraction process in the specimen. The optimized image conditions are characterized by the minimum of the differences between dynamical and kinematical phases applying suitable defocusing (KPF concept). Computed tables of HREM patterns show that optimum defocus values can be found for appropriate crystal thickness ranges. Restoring the phases of the

0304-3991/89/$03.50

structure amplitudes causes HREM images, which may be interpreted in terms of the projected crystal potential.

2. Method

For theoretically investigating the contrast features of compound semiconductors under medium-voltage HREM conditions ($V = 400$ kV, $C_s = 1$ mm), the "multi-slice" algorithm [5,6] is used, where the electron-optical imaging conditions are considered by the contrast transfer function (CTF). Besides some studies of the (100) specimen orientation (fig. 6), the present considerations are concerned with the (110) axis of the crystalline samples. In the (110) diffraction pattern there is a non-centrosymmetric behaviour of the reflections with respect to intensity and phase oscillations, which is not observed in the (100) direction.

The intensity and the phase of the kinematical structure amplitudes are defined in such a way that their Fourier synthesis provides the (projected) crystal potential. The structure amplitudes are specified for a ZnS cell in table 1 (all mixed-type amplitudes are zero).

Studying very thin crystals (kinematical approximation) by electron microscopy yields interpretable images of the crystal potential in the Scherzer focus within the attainable point resolution. Under this focus condition the relative phases of the structure amplitudes are maintained by the broad band of nearly constant phase transfer (CTF $= -$i, $\pi/2$ phase shift). With an increasing specimen thickness the diffracted reflections (intensity $I(hkl)$, phase $\Phi(hkl)$) oscillate according to their deviation from Bragg-excitation ($s \propto d^{-2}$ in the symmetric Laue case). If the aberration-free focus condition, i.e. CTF$(u_{hkl}) = 1$, can be fulfilled at the spatial frequencies u_{hkl} of the reflections, the phases of the reflections are not modified during the imaging process (excluding multiples of 2π). Thus the aberrations are banished between the reflections for a small number of $1/d$ values so that for monatomic crystals (Au [7], Si [8,9]) structure-like images may be obtained for an appropriate specimen thickness (e.g. $t \approx \xi_{000}/2$). For "multi"-component structures, however, optimum HREM imaging conditions can be realized neither by the Scherzer focus nor by the aberration-free condition. Both concepts fail because of the non-proportional phase change with increasing thickness due to the dynamical interaction, especially in the case of non-centrosymmetric systems. But, in the same experimental probability, it should be possible to reconstruct the phases of the structure amplitudes for the transferred reflections applying an adapted CTF during the imaging process. Such an optimized CTF can be found if the actual phase of the strong reflections are known.

Therefore the basis of the CTF optimization is the determination of the dynamical behaviour of intensities and phases of the diffracted electron waves.

The following simulations are carried out including 97 diffracted beams (routine conditions). They are verified by "multi-slice" computations with 1119 and 2091 Fourier coefficients; the match as well as the modifications of the results are discussed in figs. 1 and 5. For both the assumed numbers of Fourier coefficients the interpretation of the thickness-intensity profiles of the InP reflections reveals that the reflections (hkl) and $(\bar{h}\bar{k}l)$ with $l \neq 0$ differ for an increasing specimen thickness t, i.e.: $I_{hkl}(t) \neq I_{\bar{h}\bar{k}\bar{l}}(t)$ and $\Phi_{hkl}(t) \neq \Phi_{\bar{h}\bar{k}\bar{l}}(t)$ (I = intensity and Φ = phase). The $I(t)$ functions and the $\Phi(t)$ curves in fig. 1 show that reflections in diametric position to the primary spot seem to oscillate opposite to each other, losing the original phase difference.

"Multi-slice" calculations for GaAs and InP have indicated that the intensity ratio and the phase difference between (hkl) and $(\bar{h}\bar{k}l)$ with

Table 1
Structure amplitudes of A_3B_5 compounds with ZnS cell

$F(hkl)$	(hkl) of (110) axis	(hkl) of (100) axis
$4\{f(A)+f(B)\}$	$(2\bar{2}0)$, (004),...	$(0\bar{2}2)$, (004),...
$4\{f(A)-f(B)\}$	(002), $(2\bar{2}2)$,...	(002),...
$4\{f(A)+if(B)\}$	$(\bar{1}11)$, $(1\bar{1}1)$, $(\bar{1}1\bar{3})$, $(1\bar{1}\bar{3})$,...	
$4\{f(A)-if(B)\}$	$(1\bar{1}\bar{1})$, $(\bar{1}1\bar{1})$, $(\bar{1}13)$, $(1\bar{1}3)$,...	

A: Ga, In; B: As, P.

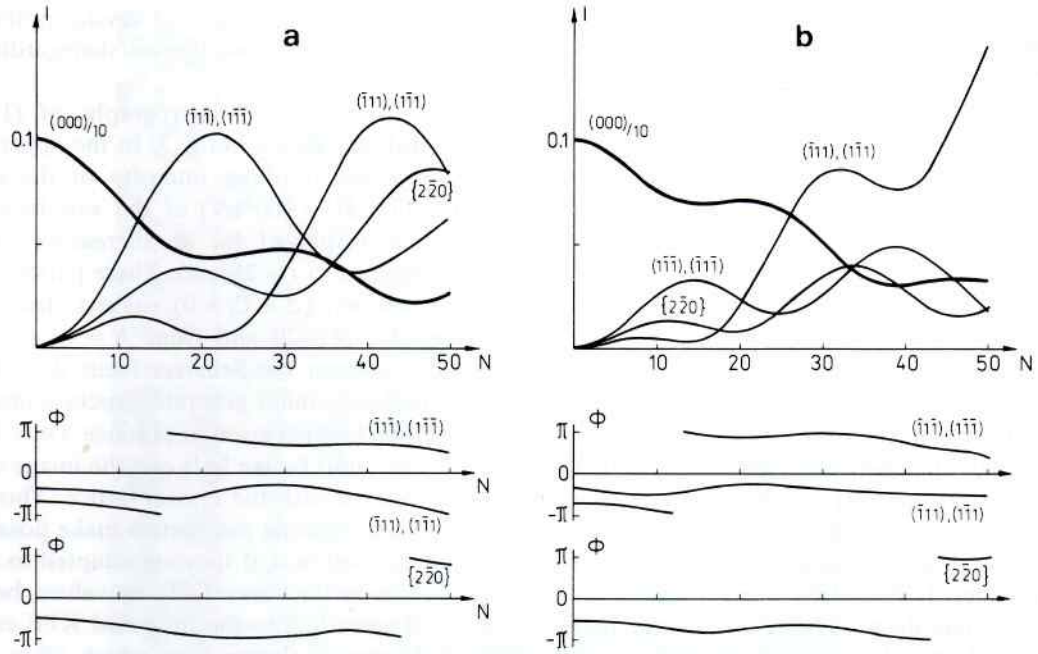

Fig. 1. Intensity profiles and phase plots of reflections (hkl) for InP(110) computed by the "multi-slice" algorithm; crystal thickness: $t = N\Delta z$ ($\Delta z = 0.415$ nm). (a) NBEAM = 97, (b) NBEAM = 1119.

$l \neq 0$ depend on the quotient of atomic scattering factors of the A_3 and B_5 components (GaAs: $f(\mathrm{Ga})/f(\mathrm{As}) = 0.96$, InP: $f(\mathrm{In})/f(\mathrm{P}) = 1.9$). The depth oscillations of the reflection intensities ("Pendellösung") for monatomic diamond cells in symmetric Laue case show identical behaviour for all reflections with the same $1/d$ value. The degeneration of this phenomenon for compound semiconductors as a function of the ratio of the scattering factors discussed above can be interpreted as a failure of the Friedel law for non-centrosymmetric crystals in many beam interactions.

On the understanding of this complicated dynamical phase behaviour of the strong reflections $\Phi_t(u_{hkl})$, determined for the given crystal thickness t, the phase relations of the structure amplitudes $\Phi_{\mathrm{kin}}(u_{hkl})$ for the reflections used in imaging can be restored applying suitable focus conditions (kinematical phase focus condition, KPF). Thereby the phase shift in the electron microscope $\Phi_{\mathrm{CTF}}(u_{hkl})$, described by the CTF and controlled by defocus Δ, becomes numerically optimized so that the quadratic deviations of phase differences attain a minimum at the reflections ($u_{hkl} = 1/d_{hkl}$; $u_{hkl} = (h^2 + k^2 + l^2)^{1/2}/a$ for cubic crystals). The optimized defocus Δ_{opt} is the solution of the following KPF condition (see ref. [10] and appendix):

$$\sum_{hkl} \{ \Phi_t(u_{hkl}) + \Phi_{\mathrm{CTF}}(u_{hkl}) - \Phi_{\mathrm{kin}}(u_{hkl}) - \Phi_{\mathrm{const}} \}^2 = \min. \quad (1)$$

This relation of the phase of the reflections – as a criterion of structure imaging – must be applied to the crystal thickness t under consideration. If the sum of the quadratic deviations in the phase equation can be sufficiently minimized for all strong reflections, this procedure allows the generation of HREM patterns, which can be interpreted in terms of the projected potential. Specimen thickness intervals, which are appropriate for structure imaging, are found to be in the surrounding of the intensity minima of the primary reflection: GaAs: $5 < t < 16$ nm; InP: $4 < t < 10$ nm; $16 < t < 20$ nm. The formula for calculating the structure amplitudes in the zincblende cell (see table 1) reveals the possibility of utilizing the varying combinations of the A–B items for identifying the differ-

Table 2
List of defocus periods, which cause a 2π phase shift of the corresponding reflections

(hkl)	$1/d$ (nm^{-1})	Δ period (nm)
(111)	2.951	139.7
(002)	3.407	104.8
(220)	4.818	52.4
(113)	5.650	38.1
(004)	6.814	26.2

ent atomic species in the image contrast. In HREM studies of InP(100) for a crystal thickness corresponding to the maximum of (002), the two sublattices can be distinguished (see ref. [1] and fig. 6). In the literature [11] maxima of reflections, arising from selective structure amplitudes, are applied, e.g., to investigate the position of oxygen in metal oxides. It should be mentioned here that there is no longer the possibility of structure imaging (projected crystal potential) for these particular specimen thickness ranges.

For the given parameters ($V = 400$ kV, $C_s = 1$ mm) and the required resolution (0.14 nm), the optimized CTF exhibits 4 to 7 oscillations (see table 2).

Contrast phenomena, known for silicon ("dumbbell-contrast"), are an adequate guiding principle for GaAs and InP crystals due to their similar structures (ZnS cell).

3. Results

In fig. 2 simulated HREM images of GaAs(110) for 400 kV are presented. The assumed crystal thickness $t = N\Delta z$ is linearly increasing up to 28 nm. For most of the specimen thicknesses, "dumbbell" contrast is obtained if the images are calculated using one of the KPF-optimized defocus values (lower row). In the upper row, the image intensity is displayed for a so-called aberration-free microscope ($\Delta = C_s = 0$), i.e. the amount of the wave-function at the exit surface of the specimen, for comparison. There is no possibility of identifying the type of atoms (Ga/As) of the corresponding atom columns in the HREM micrograph. Neither appropriate experimental HREM parameters nor the projected crystal potential itself discriminate the two species, disregarding their local separation.

Calculated HREM micrographs of (110)-oriented InP are shown in fig. 3. In the upper row of the table the resulting intensity of the electron interaction ($V = 400$ kV) at the exit face of the crystal is displayed for an increasing specimen thickness (up to $t = 28$ nm). These patterns of the wave function ($\Delta = C_s = 0$) suggest structure-like images for $N = 20$ and from $N = 40$ to $N = 50$. Conditions near the Scherzer focus $\Delta_s = 48.5$ nm (middle row) cannot generate structure images for crystal thicknesses given in practice. Only for very thin ($t \leq 2$ nm) fictive foils can the image contrast be correlated with the crystal lattice. This proves that the microscope parameters make possible the required resolution, if they are adapted to a variable specimen thickness. Defocus values, being optimized according to the proposed KPF criterion, provide images (lower row) which allow one to reproduce the projected crystal potential under the conditions discussed; contrast reversal and "dumbbell"-type patterns are typical characteristics.

Fig. 4 deals with the question under which conditions atomic columns of In and P in the sample may be distinguished by HREM. For an appropriate crystal thickness ($N = 20$), all KPF-defocus values, determined in the described way for the range of $-100 < \Delta < 200$ nm, are applied to compute half-tone patterns (middle row). Furthermore, in this figure the defocus values are varied in the nearest surrounding of these optimized CTFs. Due to the phase conditions, around $\Delta = -40$ nm and $\Delta = 170$ nm, the nearly symmetrical "dumbbells" are deformed. With all the other parameters being kept constant, In and P seem to alter their places in the calculated contrast if one presupposes that the heavier In atoms appear larger and brighter in the image. In addition, the virtual interatomic distances in the images are influenced by through-focusing. An unambiguous distinction of the In and P atoms by this kind of HREM experiments thus requires the support of image simulations to clarify the through-focus tendencies with respect to the A–B component contrast, including a possible specimen tilt.

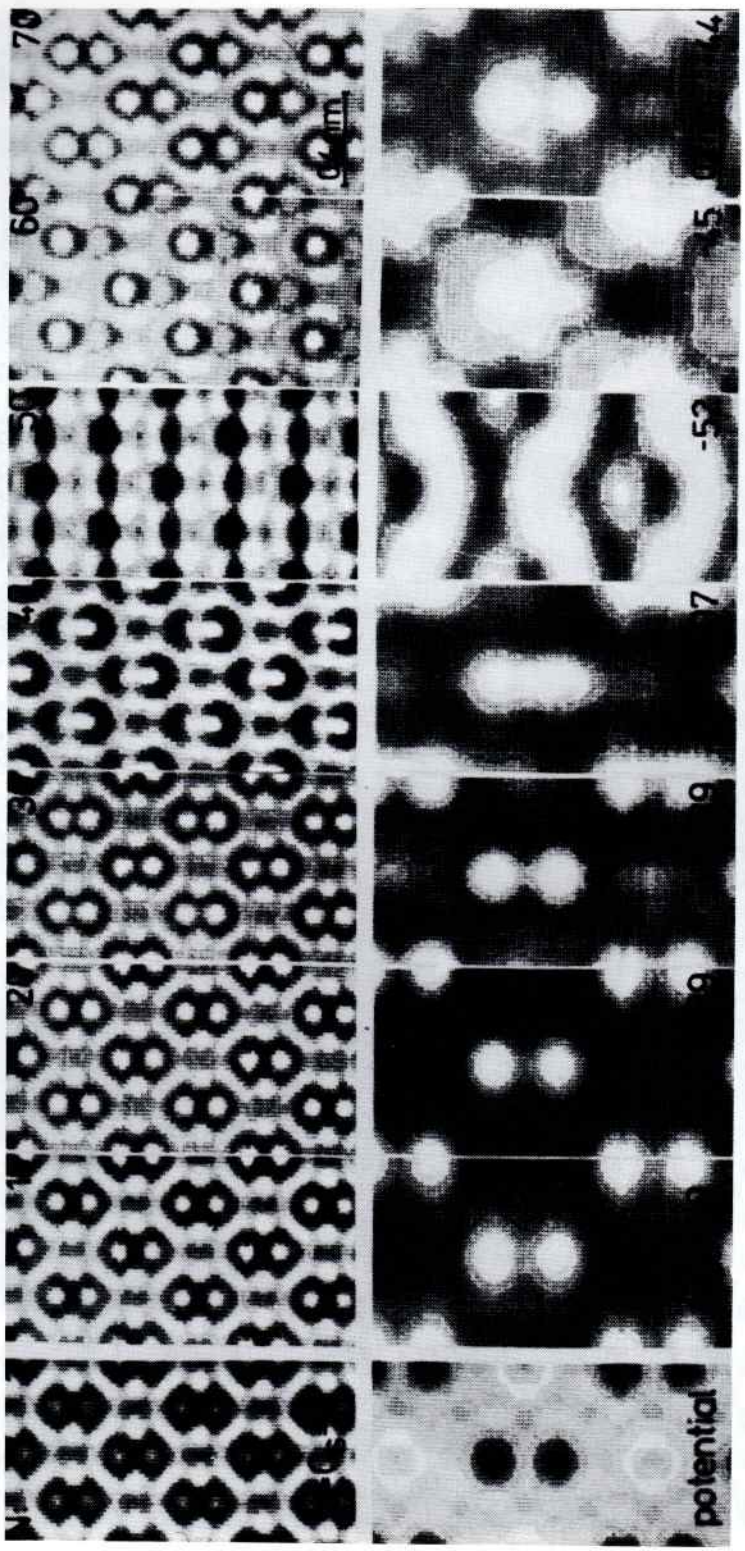

Fig. 2. HREM simulations for GaAs(110), $V = 400$ kV. Top: wave function at exit surface ($\Delta = C_s = 0$); bottom: defocused images, $C_s = 1$ mm, Δ_{opt} (in nm), $\delta f = 3$ nm
Crystal thickness: $t = N\Delta z$ ($z = 0.399$ nm).

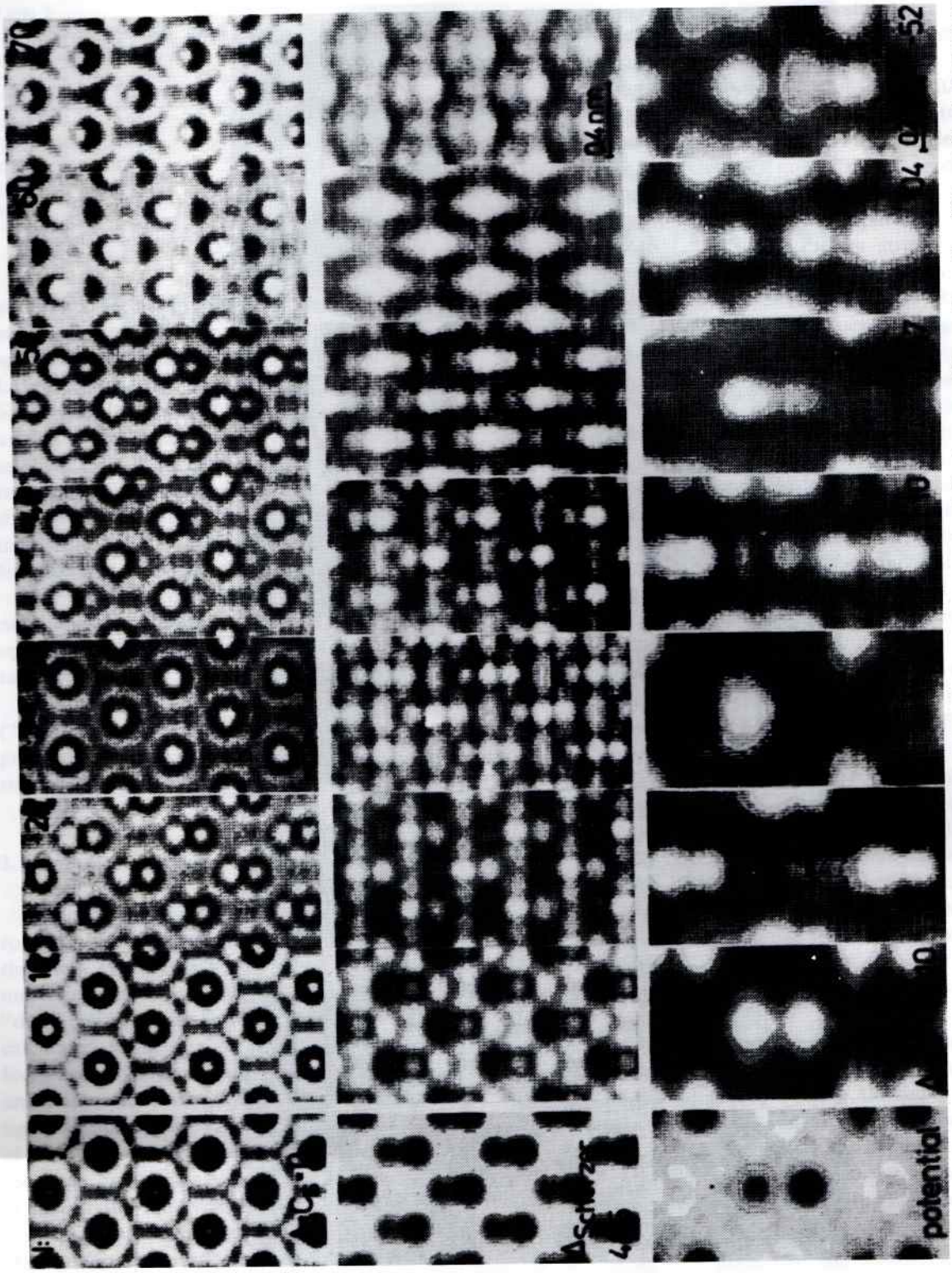

Fig. 3. HREM patterns for InP(110), $V = 400$ kV. Top: wave function at exit surface ($\Delta = C_s = 0$); middle: images at Scherzer focus ($\Delta = 48.5$ nm), $C_s = 1$ mm; bottom optimized images, $C_s = 1$ mm, Δ_{opt} (in nm), $\delta f = 3$ nm. Crystal thickness: $t = N\Delta z$ ($\Delta z = 0.415$ nm).

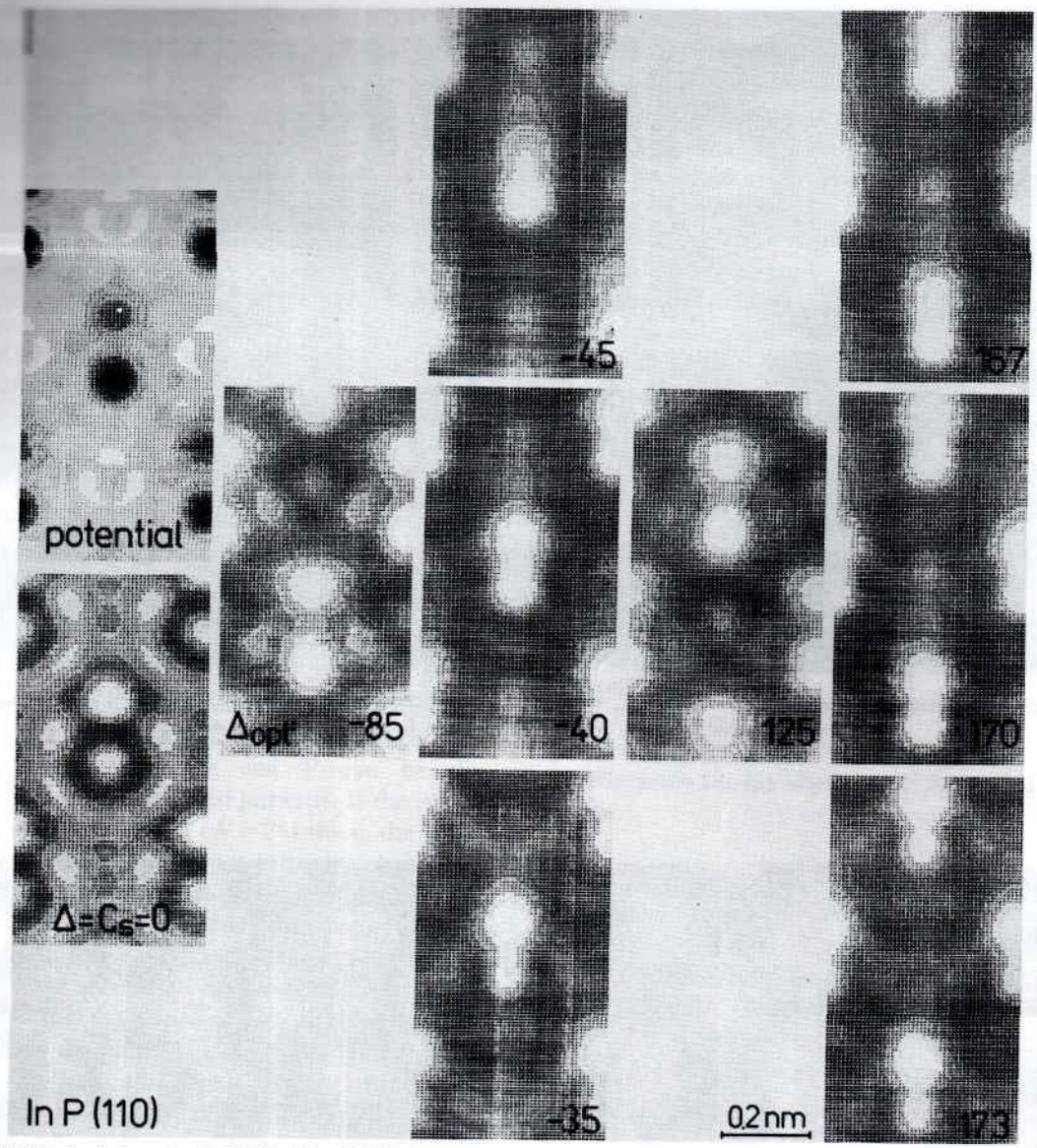

Fig. 4. HREM simulations for InP(110), $V = 400$ kV. Parameter: crystal thickness $t = 8.4$ nm, $C_s = 1$ mm, optimized defocus Δ_{opt} ($-100 < \Delta_{opt} < 200$ nm). (Test of element distinction by focus variation.)

The HREM patterns simulated in fig. 5 are calculated for an increased number of diffracted beams (NBEAM = 1119) to compare the results with the limited beam-number calculations in figs. 3 and 4. The upper row of fig. 5 correlates directly with fig. 4, whereas the bottom row is comparable with columns $N = 40$ and $N = 50$ in fig. 3. The numerical description of the electron diffraction process is sensitive to the number of reflections included (cf. fig. 1). The highly resolved "multi-slice" calculations were carried out to verify the discussed considerations. According to the very large number of interacting beams, the dynamical extinction distances become shorter, but in principle the features are maintained, because they are preferentially controlled by the low-order reflec-

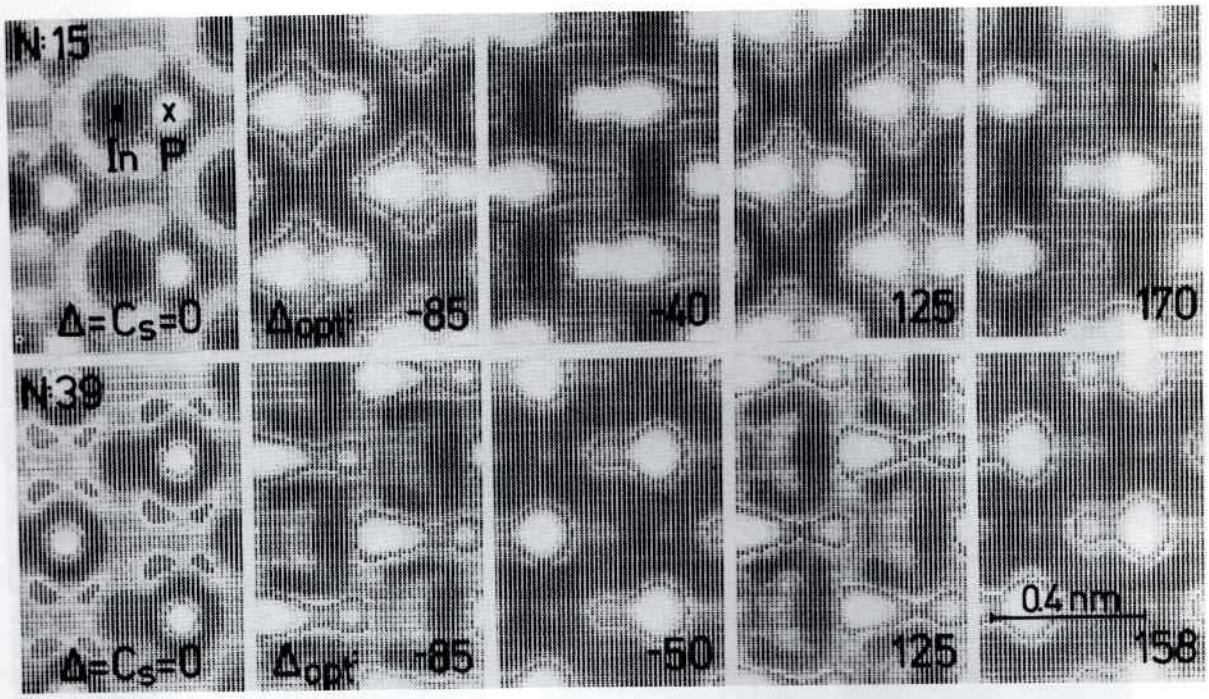

Fig. 5. HREM simulations for InP(110), $V = 400$ kV, $C_s = 1$ mm. Number of considered beams: 1119, $\Delta z = 0.415$ nm. Top: $t = N\Delta z$, $N = 15$; bottom: $t = N\Delta z$, $N = 39$. Optimized defocus values Δ_{opt} (in nm).

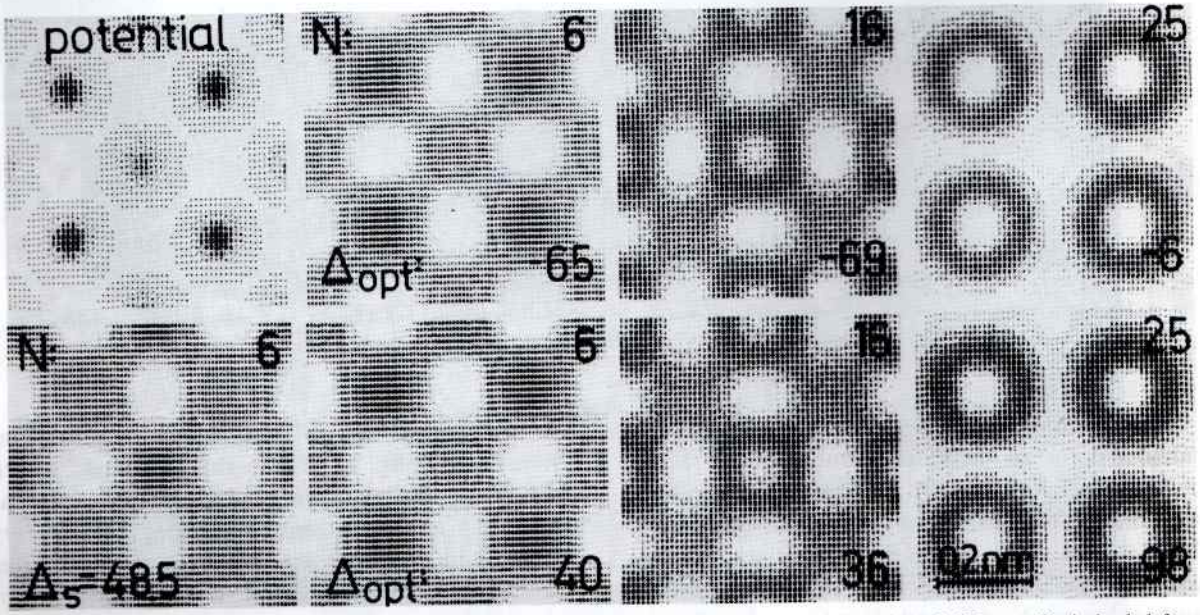

Fig. 6. HREM simulations for InP(100), $V = 400$ kV, $C_s = 1$ mm; crystal thickness: $t = N\Delta z$, $\Delta z = 0.587$ nm. Optimized defocus values Δ_{opt} (in nm).

tions. While the specimen thickness interval under investigation is slightly enlarged by the varying number of beams, the imaging parameters are mainly determined by the $1/u^2$ spectrum and the structure amplitudes.

The electron diffraction and image formation of (100) oriented InP crystals is discussed in fig. 6. For this orientation the "multi-slice" calculations resulted in a centrosymmetric behaviour of the reflection intensities and phases with increasing specimen thickness. Optimized defocus parameters (KPF) are used, considering {002}, {022}, and {004} reflections. For very thin crystals ($N = 6$), the contrast with the defocus values determined ($\Delta_{opt} = -65$ nm and 40 nm) is similar to the images in the Scherzer focus ($\Delta_S = 48$ nm); the distinction of the two atom species is improved, however, by the KPF value (In darker than P). In the literature [1] the (100) orientation near Scherzer focus is preferred for identifying sublattices; the present simulations reveal the reason for the small change of focus from the Scherzer value to the KPF optimum (40 nm). For $N = 16$, the intensities of the {002} and the {022} reflections are comparable; nevertheless In and P can be distinguished in the calculated patterns. If the crystal is approximately 14 nm ($N = 25$) thick, the {002} reflections are of maximum intensity. According to the formula of the scattering factor (see table 1), one has to expect maximum distinction between the In and P contrasts: In atoms are imaged as dark rings around a bright centre.

Comparing the two orientations discussed for InP reveals that there are some fundamental differences for crystallographic reasons. Unlike the (100) axis, the electron diffraction in (110) direction has a non-centrosymmetric behaviour. Because of the intensity and phases of the corresponding reflections in the (110) diffraction pattern in HREM imaging solely reversed contrast is observed.

4. Conclusions

The method of optimizing the HREM-imaging parameters of crystalline samples (KPF concept), proposed here, consists in the phase restoration of the diffraction reflections by suitable focusing with respect to the kinematical structure amplitudes. For appropriate specimen thickness regions, i.e. an adequate intensity ratio of the reflections, the calculated image contrast is interpretable in terms of the projected crystal potential. Unlike the usual criteria of a HREM parameter fit, this technique certainly requires a simultaneous computer simulation. For the given crystal data, orientation and thickness, the defocus can only be optimized if the intensity and phase of the reflections are known. A through-focus series of an inspected specimen region has to take into account the expected specimen thickness interval; wedge-shaped crystals are desirable for practical work. The KPF concept, here applied to restore the kinematical phases and the crystal potential, can be generalized to such phase modifications that allow one to gain additional specimen information by HREM.

Acknowledgement

The authors wish to thank Prof. Dr. J. Heydenreich for his interest and for useful discussions.

Appendix

The KPF condition (1) may be written more generally

$$S = \sum_j g_j^2 \left[\Phi_{CTF}(\boldsymbol{u}_j - \boldsymbol{u}_0) - \Phi_j \right]^2 = \min, \qquad (2)$$

where

$$\Phi_{CTF}(\boldsymbol{u}) = -\pi\lambda\left(\Delta - \lambda^2 C_s u^2/2\right)u^2, \qquad (3)$$

$$\Phi_j = \Phi_{kin}(\boldsymbol{u}_j) + \Phi_{cj} - \Phi_t(\boldsymbol{u}_j) - 2k_j\pi. \qquad (4)$$

The dynamical phase Φ_t and the phases of the structure amplitudes Φ_{kin} are given in the way described above in the reciprocal lattice positions $\boldsymbol{u}_j$ of the reflections. The contrast transfer function Φ_{CTF} characterizes the phase shifts in the microscope, where the parameters λ, Δ and C_s are the wavelength, defocus, and spherical aberration

coefficient, respectively (under-focus corresponds to the positive sign of Δ). Different phase shifts of reflections with identical $1/d$ values can be included by the off-axis tilt $\boldsymbol{u}_0$ of the transmitted beam. The additional phase offsets Φ_{cj} allow one to adjust other desired conditions than the kinematical phases, whereas the weighting factors g_j^2 can be chosen depending on the reflection intensity and/or on the damping envelope of the CTF. To compare different cases of optimization, the normalization $\Sigma_j g_j^2 = 1$ is preferred. The arbitrary integers k_j are chosen to fulfill the subcondition $|\Phi_{CTF} - \Phi_j| \leq \pi$, which can be realized because of the modulo 2π property of the phases.

To strictly restore the kinematical phases by KPF, vanishing additional phase offsets $\Phi_{cj} = 0$ and equally distributed weighting factors $g_j = 1/N$ are necessary. A constant phase offset $\Phi_{cj} = \Phi_c$ for all j implies a lateral shift of the projected cell; it is applied to minimize S.

With the abbreviations

$$a_j = -\lambda(\boldsymbol{u}_j - \boldsymbol{u}_0)^2/2, \tag{5}$$

$$b_j = \lambda^3 C_s(\boldsymbol{u}_j - \boldsymbol{u}_0)^4/4 + \left[\Phi_t(\boldsymbol{u}_j) - \Phi_{kin}(\boldsymbol{u}_j) - \Phi_{cj}\right]/2\pi, \tag{6}$$

the KPF condition (2) and the subcondition are transformed to

$$S(\Delta) = 4\pi^2 \sum_j g_j^2 (\Delta a_j + b_j + k_j)^2 = \min, \tag{7}$$

and

$$|\Delta a_j + b_j + k_j| \leq 1/2, \tag{8}$$

respectively. From eqs. (6) and (7) and for normalized weights, one obtains $S \leq \pi^2$ as an upper limit; furthermore, using this analytical presentation, the optimization problem can be treated separately from the physical point of view:

(i) If a_j were linearly independent in rational numbers, a Δ would always exist for which S vanishes (proof of Kronecker). But in the cases under consideration, $\boldsymbol{u}_j$ are vectors of a reciprocal lattice (or one a_j vanishes because of centering) and therefore a_j are not linearly independent, which results in $\min(S) > 0$.

(ii) For a fixed set of integers $\{k_j\}$, the condition $dS/d\Delta = 0$ determines the optimum

$$\Delta_{opt} = -\sum_j g_j^2 a_j (b_j + k_j)/Z, \tag{9}$$

which is a minimum because of

$$Z = d^2S/8\pi^2\, d\Delta^2 = \sum_j (g_j a_j)^2 > 0,$$

independent of Δ_{opt} and k_j.

(iii) The minimum Δ_{opt} of eq. (7) transforms the eqs. (8) to an inequality system for the determination of possible sets $\{k_j\}$, but a straightforward solution of this system seems to be possible only by a systematic trial-and-error technique.

(iv) A better way is to solve the inequalities (7) formally with the nearest integer function $k_j = -\text{nint}(\Delta_{opt} a_j + b_j)$, where $\text{nint}(x)$ denotes that integer which fulfills $-1/2 < x - \text{nint}(x) \leq 1/2$. With this formal solution an iteration procedure results:

$$\Delta_{opt}^{(n+1)} = -\sum_j g_j^2 a_j \left[b_j - \text{nint}\left(\Delta_{opt}^{(n)} a_j + b_j\right)\right]/Z. \tag{10}$$

(v) The iteration procedure is convergent because the coefficient of Δ_{opt} is smaller than one (alternating signs). Different initial values $\Delta_{opt}^{(0)}$ of the iteration allow one to separate different sets $\{k_j\}$ to which the solution $\Delta_{opt}^{(n)}$ converge. The absolute value $S(\Delta_{opt})$ is a criterion of the applicability of the determined KPF foci in HREM.

Note added in proof

The additional phase offsets (cf. eqs. (1) and (4) included in the KPF concept should be discussed in detail in a forthcoming paper. They determine the contrast phenomena obtained and the relation to the "true atomic image" as considered, e.g., by Bourret et al. [12] and Glaisher et al. [13], dealing with very similar problems in their papers (which were available only after submission of our manuscript).

References

[1] A. Ourmazd et al., Phys. Rev. Letters 57 (1986) 3073.
[2] A. Ourmazd, in: Defects in Semiconductors, Ed. H.J. von Bardeleben (Trans. Tech., Switzerland, 1986) p. 735.
[3] H. Hashimoto et al., J. Phys. Soc. Japan 42 (1977) 1973.
[4] T. Nishida, Japan. J. Appl. Phys. 19 (1980) 799.
[5] J.M. Cowley and A.F. Moodie, Acta Cryst. 10 (1957) 609.
[6] A.J. Skarnulis et al., J. Solid State Chem. 23 (1978) 59.
[7] H. Hashimoto et al., in: Proc. 9th Intern. Congr. on Electron Microscopy, Toronto, 1978, Vol. 3, Ed. J.M. Sturgess (Microscopical Soc. of Canada, Toronto, 1978) p. 244.
[8] K. Izui et al., J. Electron Microsc. 26 (1977) 129.
[9] J.L. Hutchison et al., in: Electron Microscopy and Analysis 1981, Inst. Phys. Conf. Ser. 61, Ed. M.J. Goringe (Inst. Phys., London–Bristol, 1982) p. 357.
[10] R. Hillebrand and K. Scheerschmidt, in: Veröff. 12. Tagung Elektronenmikroskopie, Dresden, 1988, p. 261.
[11] R. Guan, H. Hashimoto and K.H. Kuo, Ultramicroscopy 20 (1986) 195.
[12] A. Bourret et al., Phys. Status Solidi (a) 107 (1988) 481.
[13] R.W. Glaisher, A.E.C. Spargo and D.J. Smith, Ultramicroscopy 27 (1989) 19.